

Interlayer Resistance of Misoriented MoS₂

Kuan Zhou,* Supeng Ge, and Amrit De

Department of Physics and Astronomy, University of California, Riverside, CA 92521-0204

Darshana Wickramaratne

Materials Department, University of California, Santa Barbara, CA 93106-5050

Shanshan Su and Roger K. Lake†

*Department of Electrical and Computer Engineering,
University of California, Riverside, CA 92521-0204*

Interlayer misorientation in transition metal dichalcogenides alters the interlayer distance, the electronic bandstructure, and the vibrational modes, but, its effect on the interlayer resistance is not known. This work analyzes the coherent interlayer resistance of misoriented 2H-MoS₂ for low energy electrons and holes as a function of the misorientation angle. The electronic interlayer resistance monotonically increases with the supercell lattice constant by several orders of magnitude similar to that of misoriented bilayer graphene. The large hole coupling gives low interlayer hole resistance that weakly depends on the misorientation angle. Interlayer rotation between an n-type region and a p-type region will suppress the electron current with little effect on the hole current. We estimate numerical bounds and explain the results in terms of the orbital composition of the bands at high symmetry points. Density functional theory calculations provide the interlayer coupling used in both a tunneling Hamiltonian and a non-equilibrium Green function calculation of the resistivity.

Introduction: There is tremendous interest in multilayer and heterostructure stacks of transition metal dichalcogenides (TMDs) [1–24]. They exhibit strong spin orbit coupling and non-trivial topology [3–5], large Seebeck coefficients [15], tunable bandstructure [18, 19, 25], many possibilities for band engineering [26], type II band alignments [14, 17, 20], and rectifying pn junctions [7, 14, 20]. Multilayer and heterostructure growth with stacking control have been demonstrated [20–23]. Recent reviews provide an overview of the state of the art [24, 27–29].

For TMD misoriented bilayers, both experiments and simulations show that the interlayer coupling and the interlayer distance are sensitive to the rotation angle, and that the sensitivity of the coupling is very different for different valleys [11–13, 16, 25]. A small rotation angle in hetero-bilayers alters the inter-layer exciton dynamics [30, 31]. While the effects of misorientation on the geometry, electronic bandstructure, and vibrational modes of bilayer TMDs have received significant attention, the effect of misorientation on the interlayer resistivity of TMDs has not yet been studied. Recent work considered the effect of misorientation on the in-plane transport [32]. In this work, we theoretically determine the coherent electron and hole interlayer (vertical) conductance of a misoriented MoS₂ interface as illustrated in Fig. 1(a).

In MoS₂ bilayers, the low-energy electron transport takes place at the *K* valley, and the low-energy hole transport takes place at the Γ valley. This results in an extremely asymmetric response of the electron and

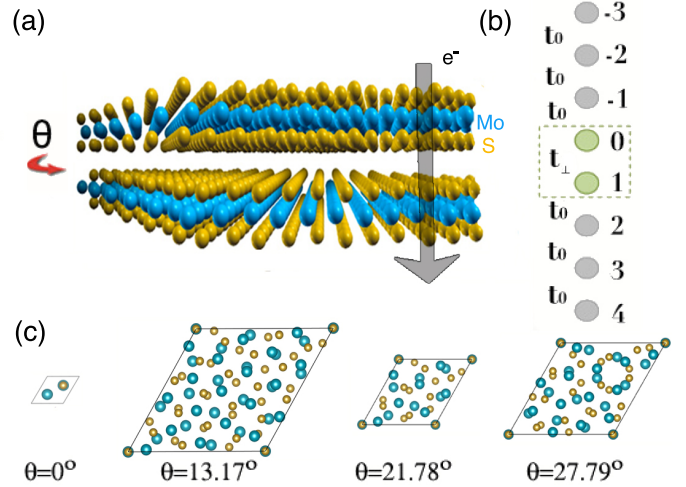


FIG. 1. (a) Atomistic geometry of the 21.78° rotated interface. The semi-transparent arrow indicates the direction of current flow. (b) Reduction to a tight binding chain model for a given valley and \mathbf{k} . The two sites 0 and 1 correspond to the two layers. (c) Commensurate unit cells corresponding to the commensurate misorientation angles.

hole interlayer conductivity to the interlayer misorientation angle. The coherent interlayer electron transport is exponentially suppressed by the misorientation, and the hole transport is only slightly affected.

Theoretical Methods: The structures considered are a 2H aligned bilayer and misoriented bilayers with commensurate rotation angles. The commensurate unit cells are shown in Fig. 1(c), and they are constructed following the method described in Ref. [33]. The rotation angles are $\theta = 13.17^\circ$, 21.78° , and 27.79° , and the cor-

* Email: kzhou003@ucr.edu

† Email: rlake@ece.ucr.edu

responding unit cell lattice constants are $\sqrt{19}a_0$, $\sqrt{7}a_0$, $\sqrt{13}a_0$ where a_0 is the lattice constant of 2H aligned bilayer equal to 3.16 Å [34]. Details of the DFT simulation input parameters and output results using the Vienna Ab initio Simulation Package (VASP) [35–39] are provided in the Appendix.

The purpose of these DFT calculations is to determine the energy splitting of the band edges resulting from the interlayer coupling. The DFT calculations are intentionally performed in the absence of spin-orbit coupling (SOC) to cleanly extract the band splitting from the interlayer coupling [19]. In the absence of SOC, the energy splitting $\Delta_\nu(\mathbf{k})$ of each band ν at wavevector \mathbf{k} due to the interlayer coupling $t'_\perp(\mathbf{k})$ is $\Delta_\nu(\mathbf{k}) = 2|t'_\perp(\mathbf{k})|$. In the basis of the eigenstates of the individual monolayers, the low-energy bilayer Hamiltonian for each band ν is

$$H = \begin{pmatrix} \varepsilon_\nu(\mathbf{k}) & t'_\perp(\mathbf{k}) \\ t'^*_\perp(\mathbf{k}) & \varepsilon_\nu(\mathbf{k}) \end{pmatrix} \quad (1)$$

where $\varepsilon_\nu(\mathbf{k})$ is the low-energy two-dimensional dispersion of band ν .

The interlayer couplings are extracted from the energy splittings near the band edge as illustrated in Fig. 2. A semi-log plot of the values versus supercell lattice constant is shown in Fig. 3(a). It is clear from Fig. 3(a) that the interlayer coupling of the holes at Γ are little affected by the misorientation angle. The interlayer couplings of the electron and hole states at K and Σ are exponentially suppressed as a function of the supercell lattice constant. This exponential dependence of the band splitting on the supercell lattice constant is also found for the band splitting in rotated bilayer graphene [40].

Only the conduction K valley and the valence Γ valley are considered for calculating the low-energy electron and hole interlayer resistances, since HSE level calculations, which provide more accurate values for energy levels, show that the conduction band K valley lies approximately 130 meV below the conduction band Σ valley, and the valence band Γ valley lies 200 meV or more above the valence band K valley. [12, 15, 34, 41]. Once we restrict our attention to the conduction K valley, which we will denote as K_c , and the valence Γ valley, which we will denote as Γ_v , spin-orbit splitting has little effect on the inter-layer transport, since the spin splitting of the conduction band at K is 1.5 meV and the valence band at Γ is spin degenerate [42]. Since we are interested in the room temperature conductance, we ignore the small spin splitting of the conduction band. To a very good approximation, the low-energy bands within the plane (perpendicular to the transport direction) are parabolic and isotropic [42]. For the transport calculations, we treat them as parabolic using two masses, m_x and m_y , such that $\varepsilon(\mathbf{k}) = \frac{\hbar^2|\mathbf{k}|^2}{2m^*}$ with $m^* = \sqrt{m_x m_y}$. The values for the masses from DFT/HSE calculations for the holes at Γ are $m_x = m_y = 0.62m_0$ and for the electrons at K are $m_x = 0.47m_0$ and $m_y = 0.45m_0$ [43].

After extracting the interlayer coupling elements t'_\perp from the DFT calculations, we calculate the interlayer

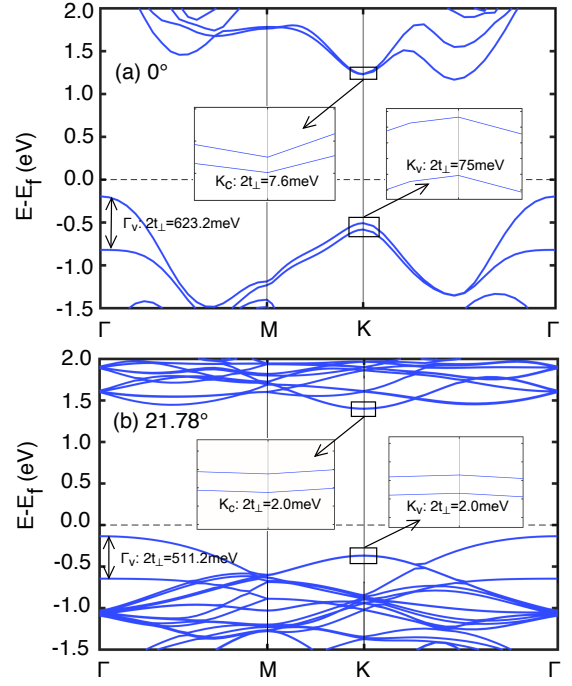


FIG. 2. DFT calculated band structures of (a) unrotated bilayer and (b) 21.78° misoriented bilayer MoS₂ in the absence of SOC. The splittings of the bands due to interlayer coupling are shown in the insets at the K points, and directly on the plots at the Γ points. The interlayer coupling parameters $t'_\perp(\mathbf{k})$ are extracted from the DFT calculations of the bilayer electronic bandstructures in the absence of spin orbit coupling.

conductance of the electron and hole bands using two different methods described below. For low energies near a given valley minimum, the standard 2D-2D tunneling formula is

$$J = \frac{g_s g_v q}{h\mathcal{A}} \sum_{\mathbf{k}} \int dE |t_\perp(\mathbf{k})|^2 A_u(\mathbf{k}; E) A_l(\mathbf{k}; E) \cdot [f(E - E_{f,u}) - f(E - E_{f,l})] \quad (2)$$

where $A_u(\mathbf{k}; E)$ is the spectral function of the upper layer, $A_l(\mathbf{k}; E)$ is the spectral function of the lower layer, $t_\perp(\mathbf{k})$ is the interlayer coupling determined from the band splitting, $f(E - E_f)$ is the Fermi-Dirac factor, and $E_{f,u(l)}$ is the Fermi level of the upper (lower) layer. In the prefactor, \mathcal{A} is the area, g_s is the spin degeneracy, and g_v is the valley degeneracy. A derivation of this expression from the standard non-equilibrium Green function expression for the current is given in the Appendix. The spectral functions are given by $A_{u(l)} = \frac{\gamma}{(E - \varepsilon(\mathbf{k}))^2 + \frac{\gamma^2}{4}} = \frac{\gamma}{E_z^2 + \frac{\gamma^2}{4}}$ where γ is the lifetime broadening in each layer and in the second equality, we define $E_z \equiv E - \varepsilon(\mathbf{k})$. Since the interlayer coupling t_\perp is a weak function of \mathbf{k} , we use its value at the band edge. Then, we can perform the sum over the transverse momenta analytically, and Eq. (2)

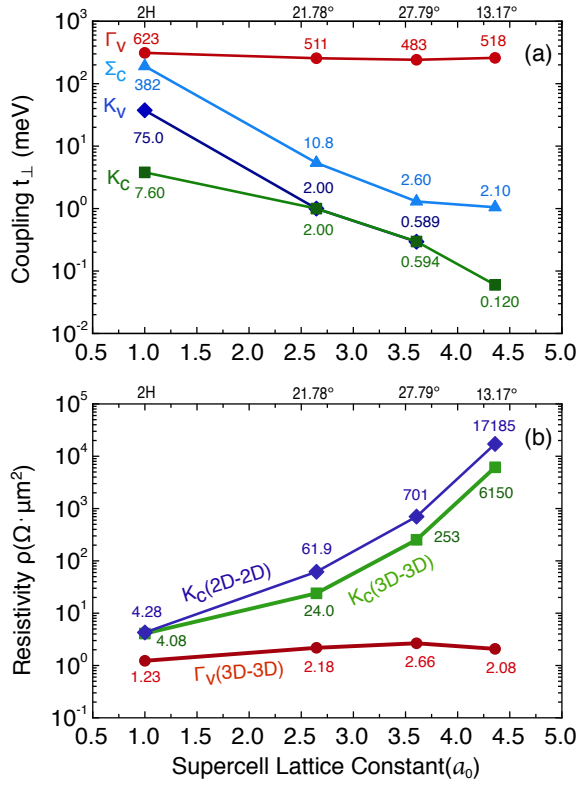


FIG. 3. (a) Interlayer coupling t_{\perp} (meV) of the conduction band valleys at K and Σ labeled K_c and Σ_c , and the valence band valleys at K and Γ labeled K_v and Γ_v . (b) Interlayer resistivity ($\Omega \cdot \mu\text{m}^2$) at the conduction (K_c) and valence (Γ_v) band edges. Both the resistivity and the coupling are plotted versus the commensurate unit cell lattice constant in units of the unrotated lattice constant a_0 . The corresponding angles are shown on the upper horizontal axis. Numerical values for the data are given next to the data points.

now has the form

$$J = \frac{g_s g_v q}{h} \frac{m^*}{2\pi\hbar^2} \int dE_z |t_{\perp}|^2 A_u(E_z) A_l(E_z) \cdot \int_0^{\infty} d\varepsilon [f(E_z + \varepsilon - E_{f,u}) - f(E_z + \varepsilon - E_{f,l})] \quad (3)$$

For small voltages, the difference in Fermi factors becomes $\frac{\partial f}{\partial \varepsilon} qV$ where V is the applied voltage, and the integral over ε gives $f(E_z - E_f) qV$ where E_f is the equilibrium Fermi level. Therefore, the 2D-2D tunneling formula for the interlayer conductivity is

$$\sigma_{2D} = \frac{g_s g_v q^2}{h} \frac{m^*}{2\pi\hbar^2} \int dE_z \frac{|t_{\perp}|^2 \gamma^2 f(E_z - E_f)}{[E_z^2 + \frac{\gamma^2}{4}]^2}. \quad (4)$$

All calculations of the electronic conductivity σ_{2D} use a value of $\gamma = 12.6$ meV, and it is estimated from the mobility lifetime using $\mu = e\tau/m^*$ and $\gamma = \hbar/\tau$. For the mobility, we chose $200 \text{ cm}^2/\text{Vs}$, which is an average of

the best measured value for a monolayer of $81 \text{ cm}^2/\text{Vs}$ [44] and the theoretical value of $320 \text{ cm}^2/\text{Vs}$ [45].

For a given transverse \mathbf{k} , the transmission resulting from this approach is $T(E; \mathbf{k}) = \frac{|t_{\perp}|^2 \gamma^2}{[(E - \varepsilon(\mathbf{k}))^2 + \frac{\gamma^2}{4}]^2}$ which has a maximum value of $16 |t_{\perp}|^2 / \gamma^2$. Since this value must be ≤ 1 , it sets an upper limit on the expression's validity in terms of the magnitude of the coupling with respect to the broadening, $|t_{\perp}| \leq \gamma/4 = 3.15$ meV. For the K_c valley, the unrotated structure does not satisfy this condition, since $t_{\perp} = 7.6$ meV; but for all non-zero rotation angles, this condition is satisfied. For the Γ_v valley at all rotation angles, it is not.

To have an expression that is also valid for the strongly coupled bands, we create a low-energy, 3D-3D transmission model for each band. Physically, this corresponds to a system of two semi-infinite stacks with one stack rotated with respect to the other resulting in the rotated interface depicted in Fig. 1(a). For each band, at each transverse \mathbf{k} , this model reduces to that of a one dimensional (1D) tight-binding chain as shown in Fig. 1(b). The hopping parameter t_0 is given by t_{\perp} of the unrotated bilayer in Fig. 2(a). For this model, the 'device' consists of the two misoriented layers numbered 0 and 1 in Fig. 1(b). The 'device' Hamiltonian for band ν is given by Eq. (1). The left and right self-energies due to coupling to the semi-infinite leads are $\Sigma^R = t_0 e^{ik_z a}$. The Green function is

$$G^R = \begin{pmatrix} E - \varepsilon_{\nu}(\mathbf{k}) - t_0 e^{ik_z a} & -t_{\perp}^{\nu}(\mathbf{k}) \\ -t_{\perp}^{\nu}(\mathbf{k}) & E - \varepsilon_{\nu}(\mathbf{k}) - t_0 e^{ik_z a} \end{pmatrix}^{-1}. \quad (5)$$

The transmission is calculated from $T(E, \mathbf{k}) = \Gamma_u \Gamma_l |G_{0,1}^R(E, \mathbf{k})|^2$ where $\Gamma_l = \Gamma_u = 2|t_0| \sin(k_z a)$. Using the dispersion relation of the leads, $E = \varepsilon_{\nu}(\mathbf{k}) + 2t_0 \cos(k_z a)$, this can be analytically evaluated to obtain $T(E_z) = \frac{t_{\perp}^2 (4t_0^2 - E_z^2)}{(t_0^2 + t_{\perp}^2)^2 - t_{\perp}^2 E_z^2}$ where $E_z \equiv E - \varepsilon_{\nu}(\mathbf{k})$. Going through the same steps as for the 2D-2D tunneling formula, the 3D-3D expression for the conductance is

$$\sigma_{3D} = \frac{g_s g_v q^2}{h} \frac{m^*}{2\pi\hbar^2} \int_{-2t_0}^{2t_0} dE_z \frac{t_{\perp}^2 (4t_0^2 - E_z^2) f(E_z - E_f)}{(t_0^2 + t_{\perp}^2)^2 - t_{\perp}^2 E_z^2}. \quad (6)$$

In all calculations of the interlayer conductance, the Fermi level is taken to be $k_B T$ below the conduction band edge when calculating the electron conductance or $k_B T$ above the valence band edge when calculating the hole conductance, with $T = 300\text{K}$. The interlayer resistivity ρ is the inverse of the conductivity calculated from Eqs. (4) or (6).

Results and Discussion: Fig. 3(b) shows the interlayer resistivity for electrons at the conduction band edge at K and the holes at the valence band edge at Γ . The interlayer resistivity for holes is only calculated from the expression for σ_{3D} in Eq. (6), since the 2D-2D tunneling formula is not valid for the holes due to the large value of $|t_{\perp}|$. The interlayer resistivity for electrons is calculated from both expressions, σ_{2D} from Eq. (4) and

σ_{3D} , and the trends and quantitative values from both expressions match to within a factor of three over 3 orders of magnitude. The agreement is not too surprising since the conductivity resulting from both expressions is proportional to t_{\perp}^2 , and the dependence of the electron and hole interlayer conductivity follows the dependence of the interlayer coupling shown in Fig. 3(a).

The physics of the interlayer coupling is determined by the periodic part of the Bloch function (the orbital composition), the phase or envelope $e^{i\mathbf{k}\cdot\mathbf{r}}$, and the interlayer trigonal arrangement of the 3 nearest neighbor Mo atoms in one layer with respect to a Mo atom in the other layer. We will first discuss the K valley and then the Γ valley.

First, consider the unrotated 2H bilayer. The very small interlayer coupling of the conduction band is due the symmetry of the conduction band Bloch functions at the K points. The conduction band edge at K is composed of predominantly Mo d_{z^2} orbitals. In a minimal basis, the Bloch state at the conduction band edge of an individual monolayer is $|K_c\rangle = \sum_{\mathbf{R}_n} |d_{z^2}; \mathbf{R}_n\rangle e^{i\mathbf{K}\cdot\mathbf{R}_n}$ where \mathbf{R}_n is the position of each Mo atom. The conduction band interlayer coupling is proportional to the the interlayer matrix element $\langle K_c, u | H | K_c, l \rangle = \langle d_{z^2}^u | H | d_{z^2}^l \rangle \sum_{n=1}^3 e^{i\mathbf{K}\cdot\mathbf{R}_n} \propto \sum_{n=0}^2 e^{in2\pi/3} = 0$ where $\langle d_{z^2}^u | H | d_{z^2}^l \rangle$ is the matrix element between interlayer, nearest neighbor, Mo d_{z^2} orbitals. Since the interlayer matrix element $\langle d_{z^2}^u | H | d_{z^2}^l \rangle$ is independent of the azimuthal angle, it is pulled outside of the sum, and the sum of the three phase factors exactly cancel. (For an expanded discussion, see the Supplementary Information of [5].)

In contrast, the valence band state at K is composed of d_{xy} and $d_{x^2-y^2}$ orbitals. The interlayer matrix elements between these orbitals change sign as a function of the azimuthal angle preventing the cancellation of the phase factors. Therefore, at the K valley of the unrotated structure, even though the conduction band orbitals are out-of-plane and the valence band orbitals are in-plane, the interlayer coupling at K_c is an order of magnitude smaller than the interlayer coupling at K_v , as shown in Fig. 3(a).

Two mechanisms compete to determine the effect of interlayer rotation on the conduction band coupling at K . When one layer is rotated with respect to the other, the symmetry is broken, and the exact cancellation of the phases is destroyed. This effect would cause the matrix element to increase. However, now the unit cell size has increased to one of the supercells shown in Fig. 1, and the interlayer matrix elements between all of the d_{z^2} orbitals in the supercell and their associated phase factors must be added. At K , the phase is changing sign approximately every lattice constant, so that as the wavefunction of the top layer is rotated with respect to that of the bottom layer, and the phases are summed over the large supercell, the matrix element is suppressed by phase cancellation. These two competing effects cause the initial slower decrease in the coupling of the conduction band at K compared to the coupling of the valence band at K

as shown in Fig. 3(a).

The effect of misorientation on the the interlayer resistivity of the electrons at K is similar to the effect of misorientation on the interlayer resistivity of electrons and holes in bilayer graphene [40, 46, 47]. The electron resistivity increases exponentially with the size of the supercell lattice constant, although the increase in MoS₂ is orders of magnitude less than the increase in bilayer graphene (compare Fig. 1d of [40] or Fig. 4 of [47] with Fig. 3(b)).

The valence band edge at Γ is composed of 28% S p_z orbitals and 67% Mo d_{z^2} orbitals[15]. These out-of-plane orbitals, especially the p_z orbitals on the surface S atoms, strongly couple between layers. Furthermore, the interlayer matrix elements are independent of the azimuthal angle, and at Γ , all of the phase factors are 1, so the matrix elements add, and the interlayer coupling is large as shown in Fig. 3(a).

When one layer is rotated with respect to the other, no phase cancellation can occur, since the Γ wavefunctions have no phase. Thus, the holes at Γ are minimally affected by layer rotation. The only effect on the hole coupling is through the slight increase in the interlayer separation causing a slight decrease in the interlayer coupling as shown in Fig. 3(a). Furthermore, the interlayer coupling of the holes monotonically decreases with angle rather than with supercell size, following the monotonic increase of the interlayer distance (see Table S1), which further indicates that different physics govern the effect of misorientation on the electron and hole interlayer coupling.

To gain perspective into what the resistivity values mean for a device application, we consider the target resistivity value of $2.5 \Omega\mu\text{m}^2$ for the emitter contact resistance required to achieve THz cutoff frequency in a heterostructure bipolar transistor (HBT) [48]. The interlayer resistivity of the holes is approximately equal to or below that value for all angles. For all non-zero rotation angles considered, the interlayer resistivity of the electrons is one or more orders of magnitude too high. This suggests design optimization of a heterostructure bipolar transistor (HBT) using stacked TMDs. A pnp HBT will be insensitive to misalignment of the layers. Furthermore, rotating the emitter layer with respect to the base layer in a pnp HBT will increase the emitter injection efficiency by one or more orders of magnitude, since the transmission of electrons injected from the base will be suppressed while the transmission of holes injected from the emitter will be unaffected.

Conclusion: The electron interlayer coupling of the conduction band at K is weak (7.6 meV), and it decreases by a factor of 63 as the supercell lattice constant increases by a factor of 4 corresponding to a 13° rotation. The hole coupling is large (632 meV) and remains large decreasing by a factor of 1.3 at a rotation angle of 27.8° The corresponding electron interlayer resistivity increases from $4 \Omega\mu\text{m}^2$ to $10^4 \Omega\mu\text{m}^2$. The hole resistivity remains near $2 \Omega\mu\text{m}^2$ for all rotation angles. Interlayer rotation between

an n-type and p-type region will suppress the electron current, which is desirable in the base-emitter junction of a pnp HBT.

Acknowledgement: This work was supported by FAME, one of six centers of STARnet, a Semiconductor Research Corporation program sponsored by MARCO and DARPA. This work used the Extreme Science and Engineering Discovery Environment (XSEDE), which is supported by National Science Foundation grant number ACI-1053575.

Appendix: Ab-initio simulation details and derivation of Eq.(2)

Electronic structure calculations of bilayer MoS₂ are carried out using density functional theory (DFT) with a projector augmented wave method and the Perdew-Burke-Ernzerhof (PBE) type generalized gradient approximation as implemented in the Vienna Ab initio Simulation Package (VASP) [35–39]. A semi-empirical Grimme-D2 correction to the Kohn-Sham energies is used to model the van der Waals (vdW) interactions [49]. Spin-orbit coupling is not included, since it has little effect on the interlayer coupling parameter, which is determined by orbital overlap. The plane wave basis energy cutoff is 400 eV. The global break condition for the electronic SC-loop is below 10⁻⁶ eV. The Monkhorst-Pack scheme is used for the integration over the Brillouin zone with a Γ centered k-mesh of 12 \times 12 \times 1 for the unrotated thin films. For rotated bilayers, k-mesh are accordingly revised to 3 \times 3 \times 1 for 13.17°, 6 \times 6 \times 1 for 21.78°, 4 \times 4 \times 1 for 27.79°, since they have different Brillouin zones. The k-space integration was carried out with a Gaussian smearing width of 0.02 eV for all calculations. All unit cells were built with 20 Å separation between replicas in the perpendicular direction to achieve negligible interaction.

The default optimization methods did not efficiently determine the bilayer separation because the van der Waals interaction energies are very small. In order to accurately determine the bilayer separation of each sys-

tem, several specific layer separations were used to optimize the structures until all or the interatomic forces are below 0.01 eV/Å as described in the Supplementary Information of [11]. The optimized structure with lower total energy was chosen for structure of each rotated angle. The interlayer distances of the relaxed structures are shown in Table S1.

The standard 2D-2D tunneling formula can be obtained following the derivation leading to the current expression of Meir and Wingreen [50]

$$J = \frac{g_s g_v q}{hA} \sum_{\vec{k}} \int dE \text{tr} \{ \Gamma_u(E; \mathbf{k}) [f(E - \mu_u) A_l(E; \mathbf{k}) + iG_l^<(E; \mathbf{k})] \}. \quad (\text{A.1})$$

For the system shown in Fig. 1(a) of the main text, A_l and $G_l^<$ are the spectral function and less-than correlation function of the lower layer, and $\Gamma_u(E; \mathbf{k}) = t_{\perp}^2(\mathbf{k}) A_u(\mathbf{k}; E)$, where $A_u(\mathbf{k}; E)$ is the spectral function of the upper layer. In a tunneling Hamiltonian approach, the two layers are assumed to be weakly coupled, so that each layer can be approximated as equilibrated with its own Fermi level. Then, $G_l^<(\mathbf{k}; E) = if(E - \mu_l) A_l(\mathbf{k}; E)$, and Eq. (A.1) becomes

$$J = \frac{g_s g_v q}{hA} \sum_{\mathbf{k}} \int dE |t_{\perp}(\mathbf{k})|^2 A_u(\mathbf{k}; E) A_l(E; \mathbf{k}) \cdot [f(E - \mu_u) - f(E - \mu_l)]. \quad (\text{A.2})$$

Angle θ	a/a_0	d (Å)	$E_{\Gamma-K}$ (eV)	E_{K-K} (eV)
2H(0)	1.0	6.2568	1.3650	1.7348
13.17°	$\sqrt{19}$	6.5142	1.5279	1.7683
21.78°	$\sqrt{7}$	6.5287	1.5339	1.7669
27.79°	$\sqrt{13}$	6.5853	1.5617	1.7698

TABLE S1. Interlayer distance (d), supercell lattice constant a , indirect energy gap $E_{\Gamma-K}$, and direct gap E_{K-K} as a function of rotation angle.

-
- [1] A. Geim and I. Grigorieva, *Nature* **499**, 419 (2013).
[2] L. Kou, T. Frauenheim, and C. Chen, *The Journal of Physical Chemistry Letters* **4**, 1730 (2013).
[3] Z. Gong, G.-B. Liu, H. Yu, D. Xiao, X. Cui, X. Xu, and W. Yao, *Nature Communications* **4** (2013), 10.1038/ncomms3053.
[4] S. Wu, J. S. Ross, G.-B. Liu, G. Aivazian, A. Jones, Z. Fei, W. Zhu, D. Xiao, W. Yao, D. Cobden, and X. Xu, *Nature Physics* **9**, 149 (2013).
[5] A. M. Jones, H. Yu, J. S. Ross, P. Klement, N. J. Ghimire, J. Yan, D. G. Mandrus, W. Yao, and X. Xu, *Nature Physics* **10**, 130 (2014).
[6] G.-H. Lee, C.-H. Lee, A. M. van der Zande, M. Han, X. Cui, G. Arefe, C. Nuckolls, T. F. Heinz, J. Hone, and P. Kim, *APL Mater.* **2**, 092511 (2014), 10.1063/1.4894435.
[7] C.-H. Lee, G.-H. Lee, A. M. van der Zande, W. Chen, Y. Li, M. Han, X. Cui, G. Arefe, C. Nuckolls, T. F. Heinz, J. Guo, J. Hone, and P. Kim, *Nature Nano* **9**, 676 (2014).
[8] Y. Gong, J. Lin, X. Wang, G. Shi, S. Lei, Z. Lin, X. Zou, G. Ye, R. Vajtai, B. I. Yakobson, H. Terrones, M. Terrones, B. K. Tay, J. Lou, S. T. Pantelides, Z. Liu, W. Zhou, and P. M. Ajayan, *Nature Materials* **13**, 1135 (2014).
[9] Q. Zeng, H. Wang, W. Fu, Y. Gong, W. Zhou, P. M. Ajayan, J. Lou, and Z. Liu, *Small* **11**, 1868 (2015).
[10] X. Zhang, F. Meng, J. R. Christianson, C. Arroyo-Torres,

- M. A. Lukowski, D. Liang, J. R. Schmidt, and S. Jin, *Nano Letters* **14**, 3047 (2014).
- [11] A. M. van der Zande, J. Kunstmann, A. Chernikov, D. A. Chenet, Y. You, X. Zhang, P. Y. Huang, T. C. Berkelbach, L. Wang, F. Zhang, M. S. Hybertsen, D. A. Muller, D. R. Reichman, T. F. Heinz, and J. C. Hone, *Nano Letters* **14**, 3869 (2014).
- [12] K. Liu, L. Zhang, T. Cao, C. Jin, D. Qiu, Q. Zhou, A. Zettl, P. Yang, S. G. Louie, and F. Wang, *Nature communications* **5**, 5966 (2014).
- [13] S. Huang, X. Ling, L. Liang, J. Kong, H. Terrones, V. Meunier, and M. S. Dresselhaus, *Nano letters* **14**, 5500 (2014).
- [14] H. Fang, C. Battaglia, C. Carraro, S. Nemsak, B. Ozdol, J. S. Kang, H. A. Bechtel, S. B. Desai, F. Kronast, A. A. Unal, G. Conti, C. Conlon, G. K. Palsson, M. C. Martin, A. M. Minor, C. S. Fadley, E. Yablonovitch, R. Maboudian, and A. Javey, *PNAS* **111**, 6198 (2014).
- [15] D. Wickramaratne, F. Zahid, and R. K. Lake, *The Journal of Chemical Physics* **140**, 124710 (2014).
- [16] C. H. Lui, Z. Ye, C. Ji, K.-C. Chiu, C.-T. Chou, T. I. Andersen, C. Means-Shively, H. Anderson, J.-M. Wu, T. Kidd, Y.-H. Lee, and R. He, *Phys. Rev. B* **91**, 165403 (2015).
- [17] A. F. Rigosi, H. M. Hill, Y. Li, A. Chernikov, and T. F. Heinz, *Nano Letters* **15**, 5033 (2015).
- [18] R. Dhall, M. R. Neupane, D. Wickramaratne, M. Mecklenburg, Z. Li, C. Moore, R. K. Lake, and S. Cronin, *Advanced Materials* **27**, 1573 (2015).
- [19] R. Dhall, K. Seyler, Z. Li, D. Wickramaratne, M. R. Neupane, I. Chatzakis, E. Kosmowska, R. K. Lake, X. Xu, and S. B. Cronin, *ACS Photonics* **3**, 310 (2016).
- [20] Y. Gong, S. Lei, G. Ye, B. Li, Y. He, K. Keyshar, X. Zhang, Q. Wang, J. Lou, Z. Liu, R. Vajtai, W. Zhou, and P. M. Ajayan, *Nano Letters* **15**, 6135 (2015).
- [21] R. Yue, A. T. Barton, H. Zhu, A. Azcatl, L. F. Pena, J. Wang, X. Peng, N. Lu, L. Cheng, R. Addou, S. McDonnell, L. Colombo, J. W. P. Hsu, J. Kim, M. J. Kim, R. M. Wallace, and C. L. Hinkle, *ACS Nano* **9**, 474 (2015).
- [22] Y. He, A. Sobhani, S. Lei, Z. Zhang, Y. Gong, Z. Jin, W. Zhou, Y. Yang, Y. Zhang, X. Wang, B. Yakobson, R. Vajtai, N. J. Halas, B. Li, E. Xie, and P. Ajayan, *Advanced Materials* (2016), 10.1002/adma.201600278.
- [23] D. Tsoutsou, K. E. Aretouli, P. Tspas, J. Marquez-Velasco, E. Xenogiannopoulou, N. Kelaidis, S. A. Giamini, and A. Dimoulas, *ACS Applied Materials & Interfaces* **8**, 1836 (2016).
- [24] A. Pant, Z. Mutlu, D. Wickramaratne, H. Cai, R. K. Lake, C. Ozkan, and S. Tongay, *Nanoscale* **8**, 3870 (2016).
- [25] P.-C. Yeh, W. Jin, N. Zaki, J. Kunstmann, D. A. Chenet, G. Arefe, J. T. Sadowski, J. I. Dadap, P. Sutter, J. C. Hone, and R. M. Osgood, Jr., *Nano Letters* **16**, 953 (2016).
- [26] C. Gong, H. Zhang, W. Wang, L. Colombo, R. M. Wallace, and K. Cho, *Applied Physics Letters* **107**, 139904 (2015), <http://dx.doi.org/10.1063/1.4932088>.
- [27] X. Xu, W. Yao, D. Xiao, and T. F. Heinz, *Nature Physics* **10**, 343 (2014).
- [28] X. Qian, Y. Wang, W. Li, J. Lu, and J. Li, *2D Materials* **2**, 032003 (2015), 10.1088/2053-1583/2/3/032003.
- [29] K. F. Mak and J. Shan, *Nature Photonics* **10**, 216 (2016).
- [30] H. Yu, Y. Wang, Q. Tong, X. Xu, and W. Yao, *Phys. Rev. Lett.* **115**, 187002 (2015).
- [31] P. Rivera, K. L. Seyler, H. Yu, J. R. Schaibley, J. Yan, D. G. Mandrus, W. Yao, and X. Xu, *Science* **351**, 688 (2016).
- [32] Y. Tan, F. Chen, and A. W. Ghosh, 'First principles study and empirical parametrization of twisted bilayer MoS₂ based on band-folding,' arXiv:1606.01858v1, June 6, 2016.
- [33] S. Shallcross, S. Sharma, E. Kandelaki, and O. Pankratov, *Physical Review B* **81**, 165105 (2010).
- [34] J. E. Padilha, H. Peelaers, A. Janotti, and C. G. V. de Walle, *Phys. Rev. B* **90**, 205420 (2014).
- [35] G. Kresse and J. Hafner, *Phys. Rev. B* **47**, 558 (1993).
- [36] G. Kresse and J. Furthmüller, *Comput. Mater. Sci.* **6**, 15 (1996).
- [37] G. Kresse and J. Furthmüller, *Phys. Rev. B* **54**, 11169 (1996).
- [38] J. P. Perdew, K. Burke, and M. Ernzerhof, *Phys. Rev. Lett.* **77**, 3865 (1996).
- [39] M. Ernzerhof and G. Scuseria, *J. Chem. Phys.* **110**, 5029 (1999).
- [40] V. Perebeinos, J. Tersoff, and P. Avouris, *Phys. Rev. Lett.* **109**, 236604 (2012).
- [41] D. Wickramaratne, 'Electronic, Vibrational, and Thermoelectric Properties of Two-Dimensional Materials,' Ph.D. Dissertation, University of California Riverside, 2015. Table A.2.
- [42] A. Kormányos, G. Burkard, M. Gmitra, J. Fabian, V. Zólyomi, N. D. Drummond, and V. Fal'ko, *2D Materials* **2**, 022001 (2015).
- [43] H. Peelaers and C. G. Van de Walle, *Physical Review B* **86**, 241401 (2012).
- [44] Z. Yu, Y. Pan, Y. Shen, Z. Wang, Z.-Y. Ong, T. Xu, R. Xin, L. Pan, B. Wang, L. Sun, *et al.*, *Nature communications* **5** (2014), 10.1038/ncomms6290.
- [45] Z. Jin, X. Li, J. T. Mullen, and K. W. Kim, *Physical Review B* **90**, 045422 (2014).
- [46] R. Bistritzer and A. H. MacDonald, *Physical Review B* **81**, 245412 (2010).
- [47] K. M. M. Habib, S. S. Sylvia, S. Ge, M. Neupane, and R. K. Lake, *Appl. Phys. Lett.* **103**, 243114 (2013).
- [48] M. J. W. Rodwell, M. Le, and B. Brar, *Proc. IEEE* **96**, 271 (2008).
- [49] S. Grimme, *Journal of Computational Chemistry* **27**, 1787 (2006).
- [50] Y. Meir and N. Wingreen, *Phys. Rev. Lett.* **68**, 2512 (1992).